Comparison of NGA-West2 Directivity Models

**Paul Spudich,[a) Badie Rowshandel,[b)] Shrey K. Shahi,[c)]
Jack W. Baker,[c)]** M.EERI, **and Brian S.-J. Chiou[d)]**

Five directivity models have been developed based on data from the NGA-West2 database and based on numerical simulations of large strike-slip and reverse-slip earthquakes. All models avoid the use of normalized rupture dimension, enabling them to scale up to the largest earthquakes in a physically reasonable way. Four of the five models are explicitly "narrow-band" (in which the effect of directivity is maximum at a specific period that is a function of earthquake magnitude). Several strategies for determining the zero-level for directivity have been developed. We show comparisons of maps of the directivity amplification. This comparison suggests that the predicted geographic distributions of directivity amplification are dominated by effects of the models' assumptions, and more than one model should be used for ruptures dipping less than about 65 degrees. [DOI: 10.1193/080313EQS222M]

INTRODUCTION

Five directivity models were developed as part of the NGA-West2 project. The goals of this paper are to compare the directivity effects on spectral acceleration predicted by each model for a set of test rupture geometries (Table 1), to compare the characteristics of the models, and to highlight the advances incorporated into each model compared to previous versions, with which the reader is assumed to be somewhat familiar. The models, their defining documents, the previous versions, and the abbreviations we use are shown in Table 2.

PROBLEMS IN THE 2008 NGA-WEST1 APPROACH TO DIRECTIVITY

In the initial Next Generation Attenuation (NGA-West1; http://peer.berkeley.edu/ngawest/) project that culminated in the 2008 issue of *Earthquake Spectra* (v. 24, no. 1), directivity was not included as an explicit term in the ground motion prediction equations (GMPEs) that were developed. Instead, directivity functions were developed (e.g., Spudich and Chiou 2008, Rowshandel 2010) as post hoc "corrections" to the median of a NGA GMPE by fitting directivity functional forms to the residuals of that GMPE. Applying these directivity corrections in practice is challenging. A problem of the post hoc "correction" process is that some GMPE developers deliberately allowed misfits to the data in order to

---

a) Earthquake Science Center, U.S. Geological Survey, Menlo Park, CA 94205
b) California Earthquake Authority and California Geological Survey, Sacramento, CA
c) Department of Civil and Environmental Engineering, Stanford University, Stanford, CA
d) Division of Research and Innovation, California Department of Transportation, Sacramento, CA

Table 1. Definition of test models for comparison of directivity predictions

Test model code	Mechanism	**M**	Dip (dg)	Rake (dg)	Bend angle (dg)	Rupture top depth (km)	Rupture length, width (km)	Hypocenter position updip from fault bottom (km)
ss1	Strike-slip	5.5	90	180	0	7	6, 5	2
ss2	Strike-slip	6.5	90	180	0	0	25, 13	2
ss3	Strike-slip	7.2	90	180	0	0	80, 15	5
ss4	Strike-slip	7.8	90	180	0	0	235, 15	5
ss5	Strike-slip	6.7	90	180	45	0	40, 13	5
so6	SS-oblique	7.2	70	135	0	0	80, 15	5
ss7	Strike-slip	8.1	90	180	0	0	400, 15	5
rv1	Reverse	5.5	45	90	0	5	6, 5	2
rv2	Reverse	6.5	45	90	0	0	18, 18	4
rv3	Reverse	6.5	45	90	0	5	18, 18	4
rv4	Reverse	7	30	90	0	0	32, 28	8
rv5	Reverse	7.5	30	90	0	0	80, 28	8
ro6	RV-oblique	7	30	135	0	0	32, 28	8
rv7	Reverse	7.5	30	90	45	0	80, 30	8

smooth their predicted motions as functions of periods. The addition of a directivity correction can undo the smoothing intended by the GMPE developers.

Exclusion of a directivity term in the GMPE also creates a problem in the statistical inference of NGA models. For example, there is a question of whether the estimated GMPE median is biased due to sampling bias in data. As directivity effects can amplify ground-motion intensity depending on the source-to-site geometry, the estimated median will be unbiased only if the data used to fit the GMPE is an unbiased representation of possible source-to-site geometries. A data set with biased sampling of source-to-site geometries may produce biased median predictions. For example, suppose the entire set of **M** 6 events in NGA data set consisted of the four recordings of the 1966 Parkfield earthquake (Figure 1). These stations were all in the forward directivity region and thus likely recorded higher than average motion at long spectral periods. On the average, the Abrahamson and Silva (2008) GMPE fits data in the forward direction well, including the probable directivity amplification in the observed ground motions. A non-directive GMPE fit to the Parkfield data would fit them on the average and hence seriously overestimate the median of a **M** 6 earthquake across the full range of possible source-site geometries. Potential directivity bias in the entire NGA-West1 data set was not systematically investigated by the post hoc directivity model developers and thus could not be completely ruled out.

PROJECT PLAN

The following discussion of the research plan is important because it helps explain how the directivity models differ. The Next Generation Attenuation West2 project (NGA-West2,

Table 2. Table of directivity models and predictors

Model	Bayless & Somerville	Chiou & Spudich[1]	Rowshandel	Shahi & Baker	Spudich & Chiou
Defined in	Bayless and Somerville (2013)	Chiou and Spudich (2013); Chiou and Youngs (2014)[1]	Rowshandel (2013)	Shahi and Baker (2013)	Spudich and Chiou (2013)
Abbreviation	bay13	cscy[1]	row13	sb13	sc13
Previous version	Somerville et al. (1997)	Spudich and Chiou (2008)	Rowshandel (2010)	Shahi and Baker (2011)	Spudich and Chiou (2008)
Predictor	f_{geom}	DPP	ξ	s, θ, d, ϕ	IDP
Directivity term	f_D	f_D	f_D	$I_{direc} \cdot \ln \text{Amp}(T, T_p)$	$\hat{f}_D$
M range	6.0–8.0	5.5–7.9	5.5–8.0	5–7.9	5.75–7.9
M taper	5.0–6.5	5.5–6.3	None	n/a[2]	None
Max distance of directivity effect, D_{max}	$R_{RUP} < 200$ km	$R_{RUP} < 70$ km	Period-dependent; 86 km at 10 s 40 km at 1 s	70 km n/a[2]	$R_{RUP} < 70$ km
Distance taper	(L or W)/2 to (L or W)	40 to 70 km	from $D_{max}/2$ to D_{max}	n/a[2]	40 to 70 km
Period range	0.5–10 s	0.4–10 s	0.5–10 s	0.6–10 s	0.5–10 s
Bandwidth[3]	Broad-band model	0.5545	0.6	$0.79*T_p$	0.6132
Allowed dip	Any	Any	Any	Any	Any
Allowed rake	Any	Any	Any	Any	Any
Allowed bend in strike	Any between segments	<90°	<90°	<90°	<90°
Centered prediction?	No	Yes	Yes	Yes	Yes
Number of empirical coefficients	2 per component per period	3	3 per component per period	3	6

Table 2. (*continued*)

Model	Bayless & Somerville	Chiou & Spudich[1]	Rowshandel	Shahi & Baker	Spudich & Chiou
Components of motion	RotD50, FN, FP	RotD50	RotD50	RotD50, model for arbitrary orientation relative to FP in Shahi and Baker (2011)	RotD50
Physical basis	Intuitive model[4] using closest point	Isochrone theory based on direct point; result for line source	Intuitive model[4] integrating over entire rupture surface	Intuitive model[4] for geometry, empirical model for impulsive near-fault ground motions	Isochrone theory based on closest point
User-adjustable non-geometric parameters	None	None	Can include specific slip distributions; can differentiate normal and reverse faults	None	None
Representative 10 s intra-event residual before/after	0.635/0.621; Section 2.9[5]	Not reported	0.601/0.559 Model I[5] 0.601/0.522 Model II[5]; Section 3.2.6[5]	Section 4.5[5]	0.662/0.580; Table 5.2[5]

[1]Chiou and Spudich DPP parameter with coefficients determined by Chiou and Youngs (2014).
[2]The Shahi and Baker (2013) model does not have linear distance tapers that go to zero adjustment at a specific magnitude and distance, but magnitude and distances ranges are provided in the above table based on the range of values associated with identified pulse-like motions, to give an idea as to the ranges over which the model may predict an adjustment.
[3]Width parameter of Gaussian function of period.
[4]Based on the principles of Somerville et al. (1997).
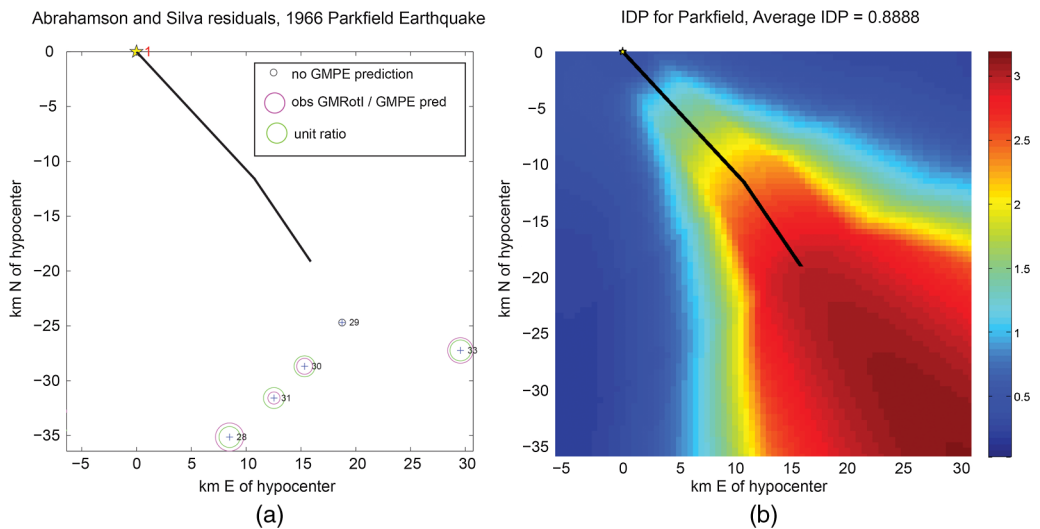[5]From Spudich et al. (2013).

Figure 1. (a) Map of 1966 Parkfield earthquake and total residuals from the Abrahamson and Silva (2008) GMPE. Black line shows fault trace, star shows epicenter. Crosses show station locations. Radius of magenta circles proportional to the residual, that is, the ratio of observed GMRotI50 (Boore et al. 2006) to GMPE prediction at 3 s period. Green circle shows 1:1 ratio, so if a magenta circle has twice the radius of the concentric green circle, the observed ground motions are twice that predicted by the GMPE. (b) Map of isochrone directivity parameter (IDP; Spudich and Chiou 2008) around the 1966 Parkfield earthquake.

http://peer.berkeley.edu/ngawest2/) considered two main approaches for developing directivity predictions for GMPEs while facing the limitations that the underlying GMPEs themselves were still under active development. Approach 1 was to include the directivity functional form in the GMPE ab initio, with its coefficients determined simultaneously (or in a parallel iterative process) with all the other GMPE coefficients (for example the distance coefficient). The Chiou and Youngs (2014) model (cscy) and the Shahi and Baker (2013) model (sb13) used this approach, although for the latter this required use of a pre-existing GMPE functional form from NGA-West1. Approach 2 was a more careful post hoc correction approach. It assumed that existing "nondirective" GMPEs already fit data containing directivity (as we have seen in Figure 1) averaged over many earthquakes. Thus, a directivity model to be added to the GMPE should be "centered," in other words constructed so that if the directivity term calculated for a rupture were averaged over potential hypocenters and racetracks having constant rupture distance, the resulting average should be zero so that the GMPE distance dependence is not modified. Centering can be either included as part of the model or performed as part of the forward application process. Models Bayless and Somerville (bay13; 2013), Rowshandel (row13; 2013), and Spudich and Chiou (sc13; 2013) have coefficients determined from data residuals from earlier generation GMPEs, but row13 and sc13 are centered, whereas bay13 is not. See Spudich et al. (2013) Section 1.3.2 for details about which directivity modelers used which type of residual (GMRotI50 or RotD50) with respect to which GMPE.

IMPROVEMENTS IN NGA-WEST2

All of the directivity models have important conceptual advances. First, all modelers except bay13 have performed extensive calculations to "center" their directivity parameters, so that the directivity model can be added to the reference GMPE without altering the overall GMPE amplification (for more details, see Chapters 3 and 5 of Spudich et al. 2013, and Shahi 2013).

Second, all the models now use distances in km rather than normalizing the dimensions to fault length, as was done by many previous directivity models, for example, Somerville et al. (1997). Use of normalized site distances led to the problem indicated in Figure 2 where a site at an angle $\theta = 0°$ off strike and a distance $s = 150$ km from the epicenter of a **M** 7.5 earthquake with length $L = 150$ km had a Somerville et al. (1997) directivity parameter $X \cos(\theta) = (s/L) \cos(\theta) = 1$, whereas a similar site 150 km from the epicenter of a 300-km-long **M** 7.8 earthquake has a directivity parameter of 0.5, meaning that it would experience half the directivity of the site 150 km from the epicenter of a **M** 7.5 earthquake.

Third, all models except bay13 are now explicitly "narrow-band" models, in which the directivity peaks at a specific period and decreases away from the peak on both sides of the peak period. The peak period itself increases with magnitude, consistent with the observed dependence of pulse period on earthquake magnitude (Somerville 2003).

DEFINITION OF RUPTURE GEOMETRY

To understand the directivity model discussion, it is helpful to understand how earthquake rupture geometry was represented in the NGA-West2 project. In particular, it is crucial to understand the distinction between a *segment* and a *fault*. A segment is a planar quadrilateral, not necessarily rectangular, slip surface having a horizontal top and bottom. A fault is a slip surface composed of multiple segments which are used to model the changes in strike direction and dip; only a single hypocenter is permitted per fault.

As is defined in Ancheta et al. (2013), a multi-segment rupture consists of two or more segments joined along their dipping edges, sharing a single hypocenter. A multi-fault rupture occurs on two or more non-contiguous surfaces (which might each be multi-segment) and each surface having its own hypocenter. Seven earthquakes in the NGA-West2 database were described as multi-fault ruptures, which required special treatment by the directivity modelers because of the multiplicity of hypocenters in each earthquake. A list of the events with multi-segment or multi-fault rupture along with the event parameters for each fault segment is included in Table A.2 in Appendix A of Ancheta et al. (2013). Directivity modelers have modeled the directivity effects due to such earthquakes differently.

Figure 2. Unequal values of Somerville et al. (1997) directivity parameter at sites (triangles) 150 km from the epicenters (stars) of a **M** 7.5 and a **M** 7.8 earthquake.

COMPARISON OF DIRECTIVITY MODELS

THE PHYSICS OF DIRECTIVITY AS MANIFESTED IN THE NGA-WEST2 MODELS

All NGA-West2 directivity models include characteristics derived from the two Somerville et al. (1997) basic insights:

- Principle 1: Ground motions are largest where the SH radiation pattern lobe (maximum in the direction of slip) aligns with the direction of rupture propagation and the direction to the site. Considering a small earthquake as a point double-force-couple source, one force-couple is aligned with the slip vectors on each side of the fault. The so-called "fault-normal" motion is aligned with the other force-couple. This principle implies that the directivity amplification will be greatest in some cone or wedge radiating from the hypocenter in the direction of rupture because both true directivity and the SH radiation pattern have narrow zones of amplification.
- Principle 2: Directivity is stronger when the distance the rupture travels is longer.

Principle 2 is less strongly grounded in theory than principle 1. Spudich and Chiou (2008) noted that full-waveform simulations of long strike-slip ruptures show that the maximum directivity amplification occurs within the ends of the fault, even for heterogeneous but statistically uniform slip distributions. Schmedes and Archuleta (2008) explained this phenomenon, for uniform homogeneous slip distributions, using isochrone theory. However, without a full understanding of this phenomenon for heterogeneous rupture, all of the directivity modelers have chosen the conservative approach of forbidding directivity amplification to decay with distance from the hypocenter along the fault trace.

A potentially important problem sidestepped by the NGA-West2 project is that there is mounting evidence that many or most large ($M \geq 7.5$) continental strike-slip earthquakes have rupture speeds exceeding the S wave speed, and such earthquakes are theoretically expected to radiate strong Mach pulses, which would have spectral content, distance decay, azimuthal distribution, and polarization different from earthquakes having more normal rupture speed. See Das (2010) for a brief review of the subject. Bizzarri et al. (2010) present theoretical models of attenuation with distance and they tentatively conclude that the few observed S wave motions that might be Mach pulses are adequately modeled by current GMPEs, but there are very few data and this is still an open question.

Both principle 1 and isochrone theory describe the directivity of S waves. However, because the peak response can occur at any time in a seismogram, the response spectra could be dominated by the S wave in some records and by surface waves in other records. Consequently, either principle 1 or isochrone theory has been applied by all the directivity modelers to both S waves, S coda, and surface waves in the data (the exception being Shahi and Baker (2011, 2013), who, by identifying pulses, are selecting for S waves).

The main physical simplification that most models (bay13, sb13, and sc13) use is the replacement of the effects of a finite fault with use of the point on the fault closest to a site of interest ("closest point"). One of the negative consequences of the use of the closest point is that its location is a discontinuous function of the site position; small shifts of the site can cause a large jump in the closest point. An example of the resulting discontinuities in IDP

is shown in Figure 3. Rowshandel's model produces the spatially smoothest maps of directivity amplification because it integrates directivity contributions from the entire fault area. To illustrate this point, a map of ξ' (Rowshandel's directivity parameter before length-denormalization and other taperings) is shown in Figure 3. The DPP parameter of
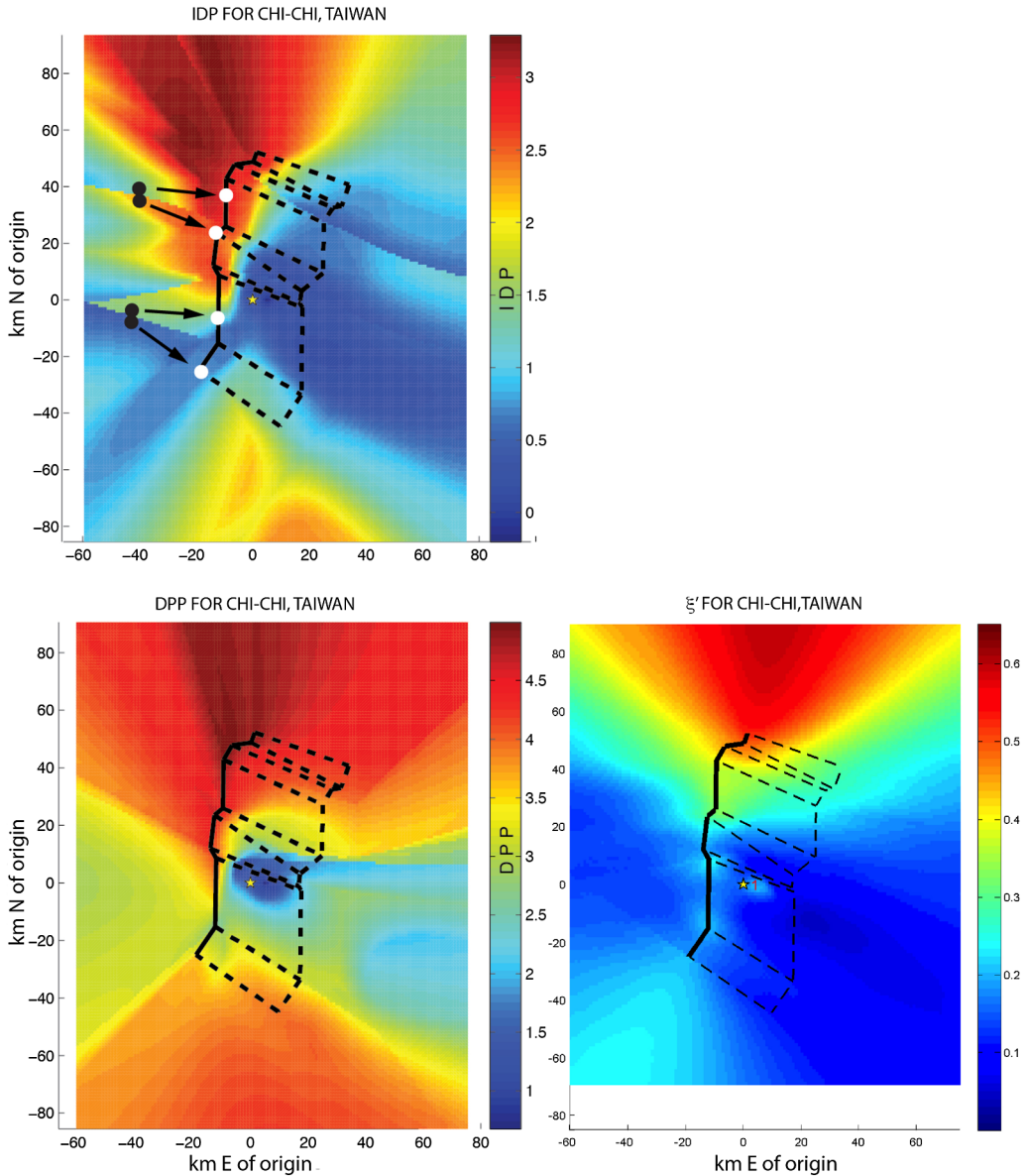

Figure 3. Maps of three directivity predictors (colors) around the Chi-Chi, Taiwan, fault trace (black solid line) and buried rupture extent (dashed lines). Upper left: IDP. Note discontinuities. White dots are closest points to pairs of sites (black dots) straddling discontinuities. Discontinuities in IDP correspond to jumps in the closest point. Right: Map of ξ', which has almost no discontinuities, owing to integration over rupture surface. Lower left: Map of DPP, which is intermediate in smoothness owing to line integral on rupture surface.

Chiou and Spudich (Figure 3) uses a line integral on the fault, and combined with its use of the "direct point," produces fewer discontinuities than are found in maps of the IDP (usually).

TEST CASES

Maps of directivity effects on near-fault ground motion predicted by several directivity models are compared for a variety of pre-determined test earthquake geometries and are summarized in this section. Test models consisted of six pure strike-slip events (ss1–ss5, ss7) on vertical faults, with magnitudes ranging from 5.5 to 8.1, one oblique slip rupture (so6) on a steeply dipping plane having magnitude 7.2, six reverse events (rv1–rv5, rv7) of $\mathbf{M}$ 5.5–7.5 on planes dipping 30°–45°, and one 30° dipping oblique slip event (ro6) of magnitude 7.0 (Table 1). All faults were planar, except for ss5 and rv7, which had 45° bends. A 45° bend is uncommon for a vertical strike-slip fault, but reverse faults having 90° bends can be found in the SCEC Community Fault Model (http://structure.harvard.edu/cfm/index.html). Hypocenters of all events were about 10% of the fault length from an end of each fault, in order to maximize directivity. The periods calculated were 1 s, 3 s, 5 s, 7.5 s, and 10 s. Not all directivity modelers made predictions for all periods or all test rupture geometries.

PREDICTIVE MODELS

Results from the five predictive models are presented in this section. The models' characteristics are listed in Table 2.

A major difference between the models is that some are broad-band and others are narrow-band (Somerville 2003). Specifically, in some of the models the period- and space-dependences of the directivity amplification are separable; that is, amplification can be written as $A(x, T, \mathbf{M}) = X(x, \mathbf{M})Y(T)$, where x is position, T is period, $\mathbf{M}$ is magnitude, and X and Y are smooth functions. In separable broad-band models like Somerville et al. (1997), $Y(T)$ is a monotonically increasing function of T. Consequently, maps of amplification for a specific earthquake at various periods look the same, except for amplitude. In narrow-band models like row13, sb13 cscy, and sc13, $A(x, T, \mathbf{M}) = X(x, \mathbf{M})Y(T, \mathbf{M})$, and $Y(T, \mathbf{M})$ is peaked at some period related to the magnitude of the earthquake. The difference between broad and narrow-band models will be evident in some of the test examples.

Another important difference is that sb13 models the response spectrum of a ground motion pulse, which is correlated with directivity but is not exactly the same thing. Pulses are expected to be big only close to ruptures, so the sb13 model has amplitudes concentrated near fault traces.

RESULTS AND OBSERVATIONS FROM TEST CASES

This section presents comparisons of spatial patterns of ground motion amplification factors, which is for each directivity model the exponential of the directivity term in Table 2. In the following plots we present contours of the amplification factor, which we refer to generically as $\exp(f_D)$. On the other hand, the colors and color-bar scale show $(\exp(f_D) - 1)$ so that if the directivity amplification for a model ranges from 70% to 120% of the nondirective motion, then the contours run from 0.7 to 1.2 while the color-bar axis runs from -0.3 to 0.2.

In the online Appendix to this paper, we define the exact quantities being mapped for each directivity model. However, it is useful here to point out the particular details that readers should have in mind when viewing the maps. The calculated amplifications are not centered for bay13, sc13, and row 13 (although the row13 and sc13 models are centered), so the calculated amplifications are with respect to an unspecified reference which varies from model to model. The plotted values of each model are not directly comparable because some are fitted to different GMPEs and residuals than others, as well as having different centering. The results presented are intended to mainly show the spatial pattern of directivity amplifications predicted by each model, not their size. One should primarily look at the spatial distributions of highs and lows. The quantity plotted for sb13 is the ratio of two GMPEs, one with directivity and one without. This ratio is not expected to be directly comparable to the other directivity model results because both the magnitude and distance dependencies change between the two GMPEs. See the Appendix and Shahi (2013) for details.

RESULTS FOR STRIKE-SLIP EARTHQUAKES

All the directivity models predict fairly similar patterns of amplification with characteristics of each model that persist over many test rupture geometries. A typical example is **M** 7.2 ss3 in Figure 4.

Unnormalized Fault Length and Scaling for Long Strike-Slip Earthquakes

A major advance of NGA-West2 was to provide a setting in which the directivity-scaling of very large earthquakes could be made more physical. A failing of directivity models that
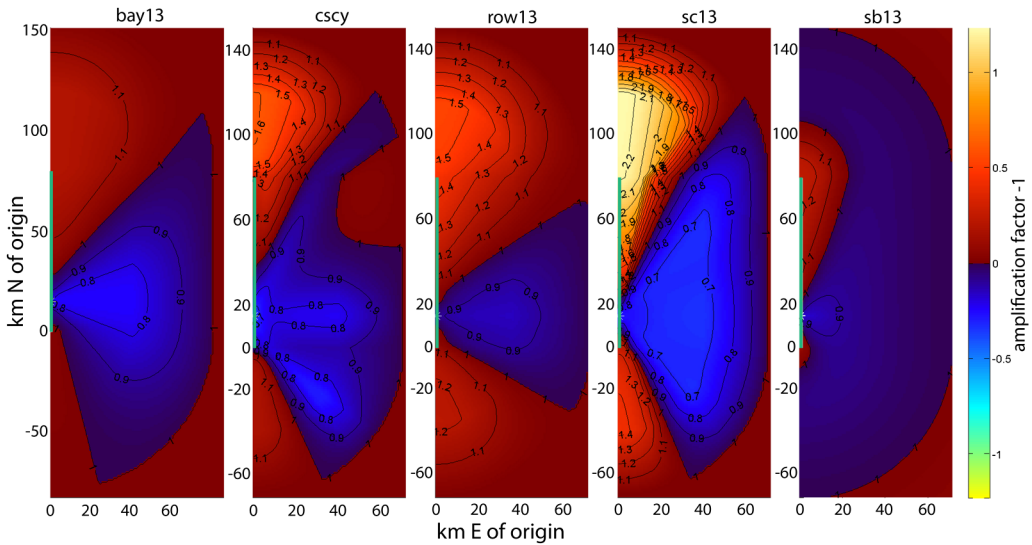

Figure 4. Ground motion amplification factor at for rupture geometry ss3, **M** 7.2, at 5 s period, comparing all models. Fault trace is turquoise line along left edge of each map. Color bar numbers are (amplification factor minus 1). This picture is fairly typical of all strike-slip test geometries. Model sb13 (right) keeps the directivity pulse amplification concentrated close to the rupture where pulses are typically found.

use forward rupture lengths normalized to total fault length, like Somerville et al. (1997), is that a site at the end of a short fault can have more directivity than a site at the end of a long fault, as shown earlier in Figure 2.

Abrahamson (2000) recognized that Somerville's model did not scale properly for long faults, and he modified the Somerville et al. (1997) directivity model by capping the X parameter to compensate. All of the NGA-West2 directivity models have been adapted to avoid this problem. In Figure 5 we show an example comparing directivity for ss4, a **M** 7.8 235 km long rupture, with directivity for ss7, a **M** 8.1 400 km long rupture. For bay13 both ss4 and ss7 show an amplification of 1.3 at about 170 km from the epicenter. Because bay13 is a broad-band model, this comparison should be exact. For narrow-band models like row13 and sc13 this comparison will be approximate because the predicted amplitude at a particular distance is a function of both magnitude and period, which are linked. We omit the comparison for sb13 and cscy because, in addition to the magnitude scaling characteristics of the former, both are centered which causes an apparent failure of the comparison.
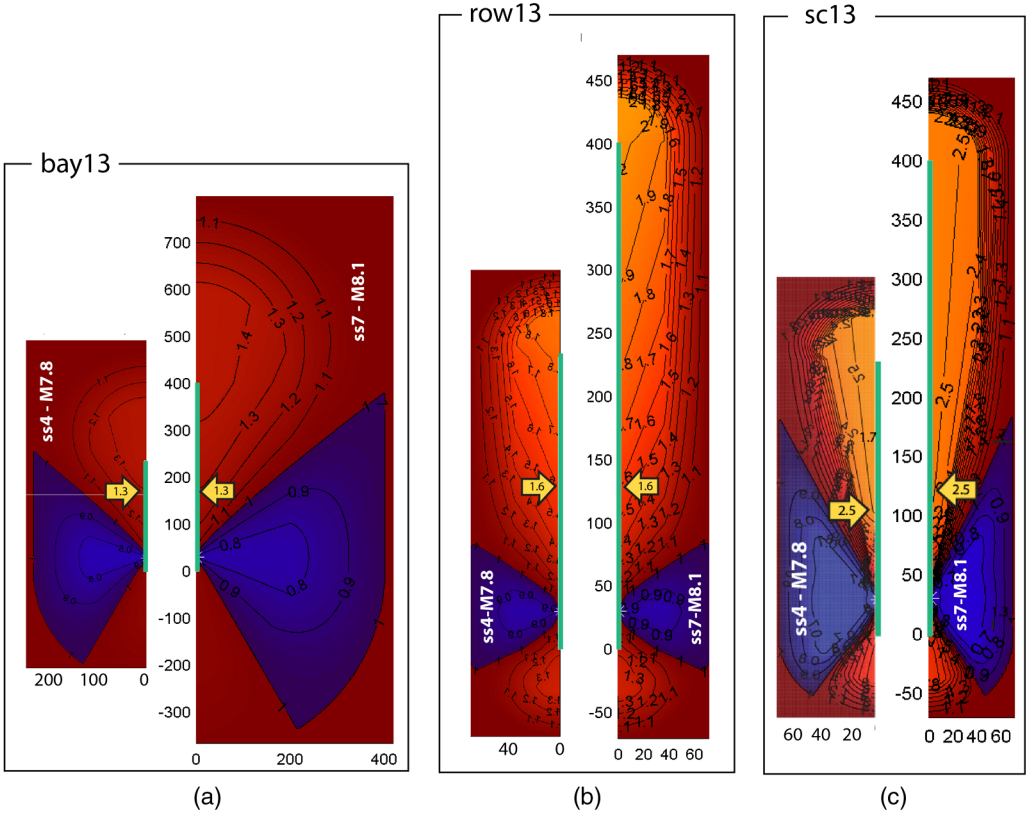

Figure 5. Maps of directivity amplification for models (a) bay13, (b) row13, and (c) sc13 for **M** 8.1 400-km-long ss7 and **M** 7.8 235-km-long ss4 at 5 s period. In each map the turquoise line along $x = 0$ is rupture trace, and the yellow arrow shows the location along strike where the labeled amplification is achieved. When the ss4 and ss7 arrows approximately align, directivity amplification is scaling properly.

It should be noted in Figure 5 that the Bayless and Somerville model predicts directivity at much greater off-strike distances than the other models. For the **M** 8.1 event, ss7, bay13 predicts directivity amplification out to 400 km perpendicular to the fault, although Bayless and Somerville recommend using the predicted directivity only out to 200 km distance, whereas all the other models do not extend much beyond 70 km.

OBLIQUE-SLIP EARTHQUAKES

Rupture geometry so6 (dip 70°, rake 135°) was modeled after the 1989 Loma Prieta earthquake geometry, which was characterized by a steep dip and oblique slip. Model sb13 has no explicit rake dependence, so the slight asymmetry seen in this model is caused by the slight non-vertical dip of the fault (Figure 6). Models sc13 and cscy have the strongest
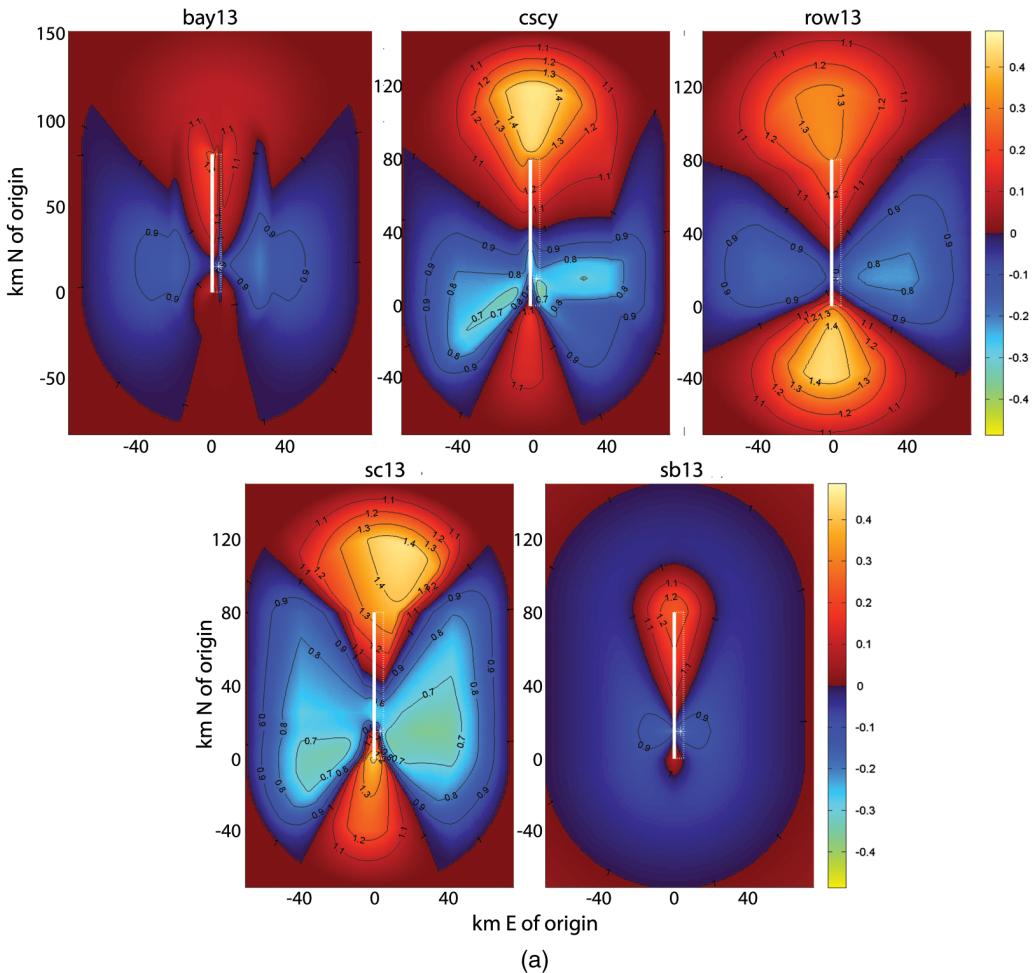
Figure 6. Comparison of predicted directivity from models bay13, sb13, sc13, and row13 at 5 s period for (a) **M** 7.2 steeply-dipping oblique-slip test model so6 and for (b) **M** 7.0 shallowly-dipping oblique-slip test model ro6.
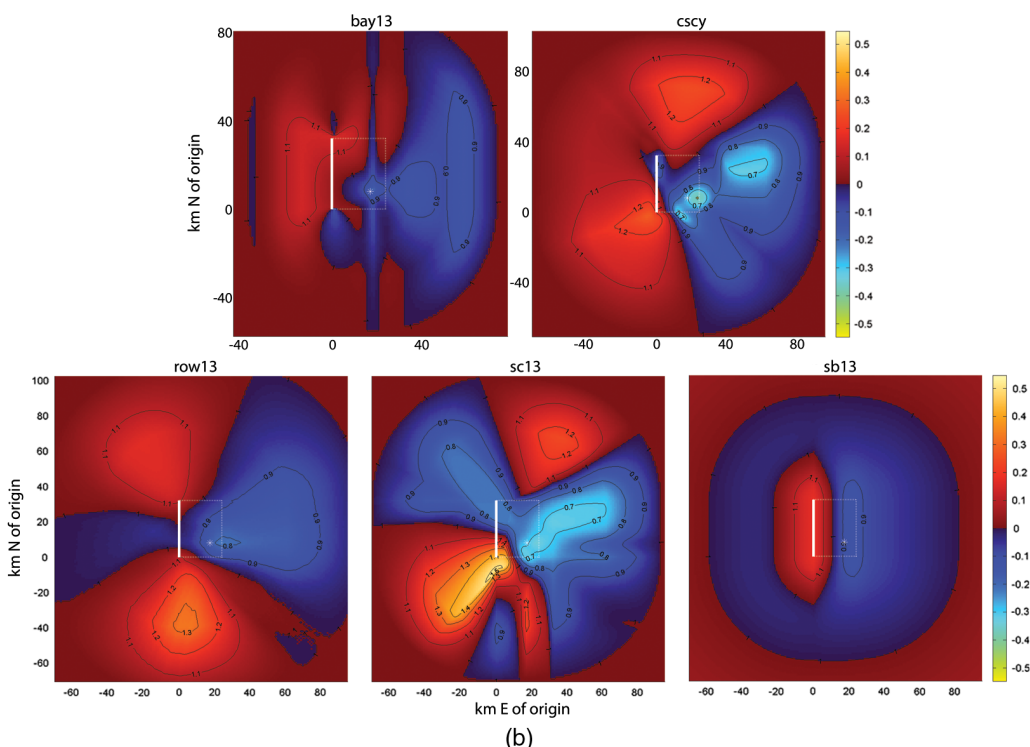
Figure 6. *Continued*.

and second-strongest rake dependences, owing to their explicit use of rake in the source radiation pattern, the former using a point source while the latter uses a line source. The strongest effect is the eastward rotation of the positive lobe north of the fault and the counter-clockwise rotation of the negative lobes south of the fault. Model row13 ground motions have an intermediate perturbation due to oblique slip. The effect of rake rotation in row13 might be diminished because the rake and rupture directions are equally weighted. Interestingly, bay13 and row13 have their large amplitudes shifted slightly west of the rupture at the north end of the rupture, while sc13 and cscy are shifted east at that location.

The effect of rake is more apparent in reverse faulting earthquake ro6 (Figure 6b), which, as in so6, has a 135° rake (viewed from above, the hanging wall moves southwest), but in contrast to so6 has a shallow dip of 30°. It is useful to compare ro6 maps with those from rv4 (Figure 7), which has the identical rupture geometry but a pure reverse mechanism.

The oblique rake causes the strongest directivity in row13 and sc13 to appear south and southwest, respectively, of the fault, surprisingly in the "backward" (shorter rupture length) direction. Model row13's use of the direction of rupture propagation as well as the slip direction probably accounts for row13's locus of maximum directivity lying east of sc13's. Model cscy's amplification pattern is a smoothed version of sc13, owing to cscy's use of a line source radiation pattern. Compared to their reverse-faulting equivalents in Figure 7,
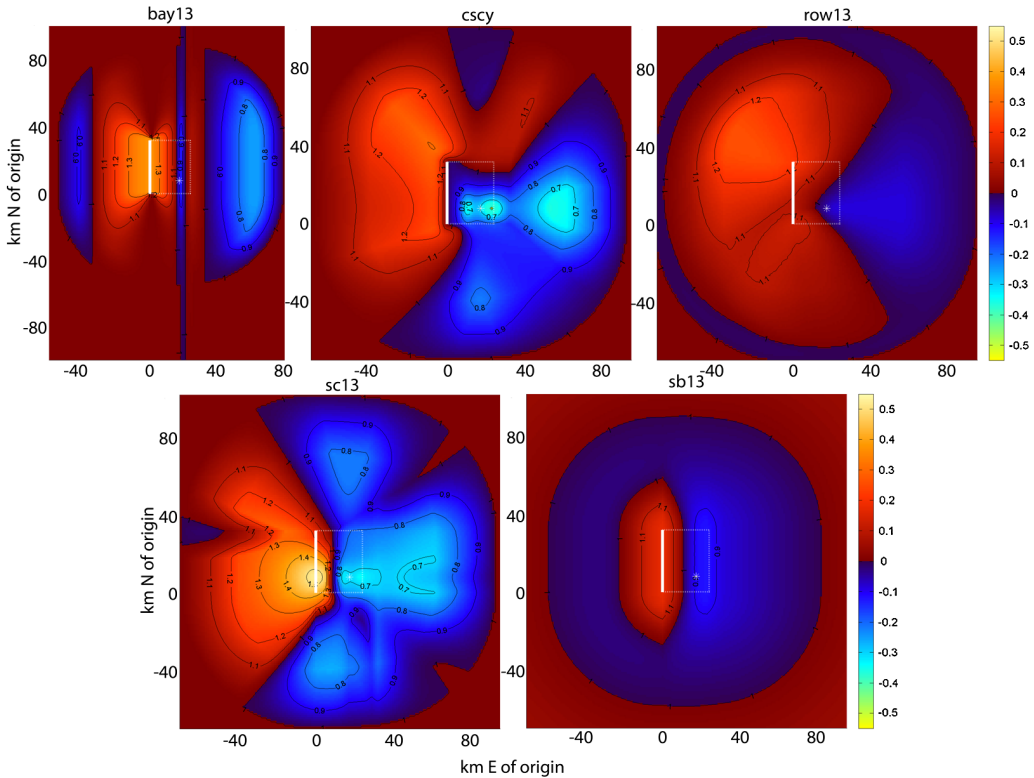
Figure 7. Comparison of predicted directivity from five directivity models for **M** 7.0 shallowly-dipping reverse fault test model rv4 at 5 s period.

bay13's ro6 amplification pattern is shifted slightly northward, and sb13 shows no difference, not being a function of rake.

There are significant differences among the predictions. Sb13 predicts maximum directivity over the center of the fault trace, where cscy, sc13 and row13 predict an intermediate level of directivity. Also row13 predicts a local maximum of directivity amplification to the NW of the rupture whereas sc13 predicts a local minimum. Forty km south of the rupture row13 has a global maximum amplification, where sc13 has a local minimum. In general, as we will discuss next, the directivity models are in poor agreement for reverse faults

REVERSE FAULTS

Rupture geometry rv4 (Figure 7) shows the characteristics common to all reverse faulting tests. Model row13 has strong directivity to the NW, caused by the length of the rupture path from the hypocenter to the NW corner of the fault. Model sc13 shares some characteristics with row13, specifically, it has a tongue of higher amplitudes radiating NW from the fault, probably caused by large D values for rupture paths from the hypocenter to the NW corner. It also has a high amplitude zone just updip from the hypocenter, caused by the

point source radiation pattern. cscy is a smoother version of sc13, and as usual, it tends to resemble row13. Results from row13 and cscy are in agreement with the results of simulation studies by Aagaard et al. (2002), who investigated directivity of near-source ground motions, in particular the impacts of dip angle and rake angle. Models bay13 and sb13, being untroubled by complicated radiation patterns, predict similar uniform directivity along the fault trace.

Only the Rowshandel model distinguishes between reverse and normal faulting. There are rupture-dynamic reasons (Oglesby et al. 2000) why near-fault motions should be higher for reverse than normal faults, and most GMPEs have mechanism-related terms that yield higher motions for reverse than for normal-faulting ruptures, so it is not clear whether directivity should also be affected by the mechanism. Oglesby et al. (2000) report that even though the stress conditions differ between reverse and normal earthquakes, the average rupture speed does not vary between the two.

The most problematic comparison is for model rv7 (Figure 8), a reverse fault with a strong bend. This test model makes clear that at least for reverse faults, the predicted spatial
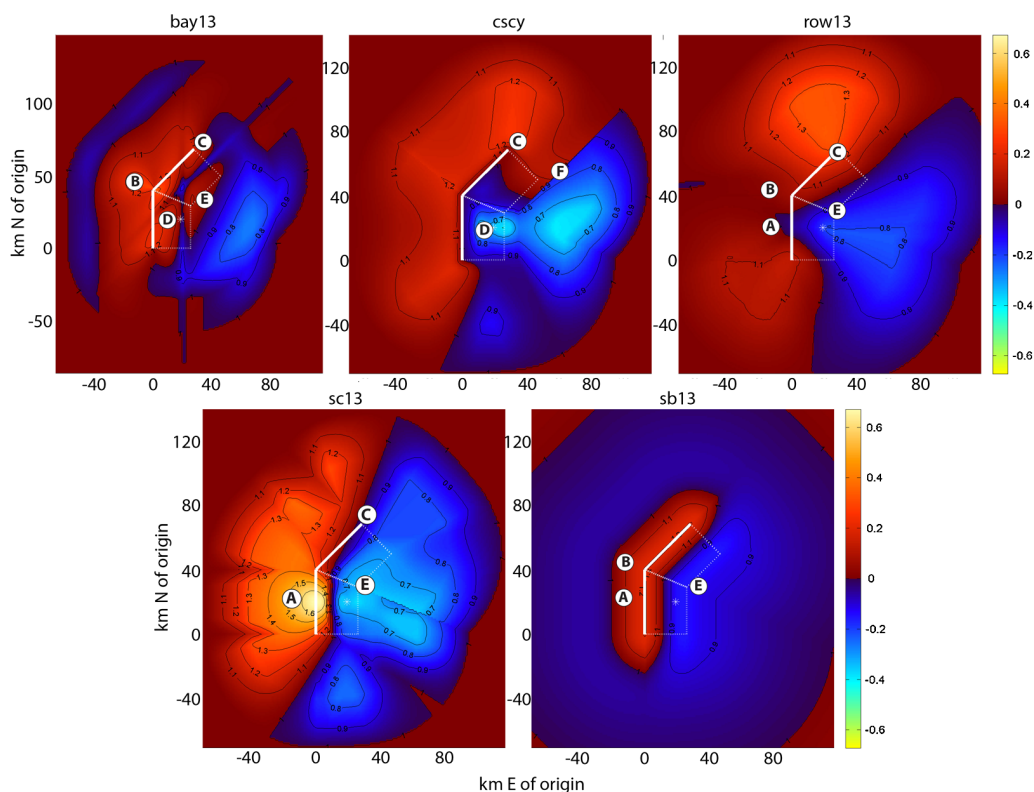

Figure 8. Comparison of all directivity models for rv7 at 5 s period, a reverse fault having a 45° bend. Letters A–F indicate locations discussed in the text. (North, east, down) coordinates of sequential vertices of rv7 are (0, 0, 0), (0, 40, 0), (28.3, 68.3, 0), (46.7, 49.9, 15), (26, 29.2, 15), (26, 0, 15) km.

patterns of directivity amplification are more controlled by assumptions of the models than they are by observed data. All models except sb13 predict higher motions on the footwall than on the hanging wall. Simulation studies by Aagaard et al. (2002) on low-angle reverse faults, also find areas of stronger directivity to be mostly in the footwall side of the faults. However, at certain points near the fault trace, the models give quite different predictions. At point A updip from the hypocenter, sc13 has its maximum directive amplification whereas row13 is medium-low. Similarly, bay13 is highest at the bend in the fault (point B) but row13 and sb13 show little amplification. Directivity is high in row13 and cscy at point C where the rupture length toward a site is long, but this point is barely amplified in sc13. In bay13 directivity is near its maximum value at point D, but near the global minimum at D in cscy. Also, at E on the hanging wall above the junction of the two bottom edges of the segments, bay13 predicts moderate amplification whereas sc13 predicts a very low value. We point out that there is a large discontinuity in the amplification at point F in cscy, which uses the DPP predictor, touted earlier as having fewer discontinuities than the IDP. Excepting the cscy unpleasantness at point F, the cscy result is smoother than the sc13 result, and it more closely resembles row13, indicating that the integration over the line source is helpful.

FAULT NORMAL, FAULT PARALLEL, AND NON-POLARIZED MOTIONS

Models bay13 and sb13 explicitly developed directivity models for specific polarizations, although sb13 also converted those predictions to RotD50 predictions to ease comparisons with other models. In addition, expressions for the polarization direction of ground motions appear in sc13, but they have not yet been thoroughly compared with data. Figure 9 shows an example of the polarization predicted by bay13. Like sc13, the use of a $\cos(2\theta)$ term in bay13 produces a radiation pattern of a point source at the hypocenter. This can be seen most clearly in the FP component, where it might be expected for a long fault with relatively uniform slip that the FP motion would be approximately constant along a line parallel to the fault trace. It should be noted that bay13 predicts FN dominance over FP far (60–70 km) from the fault.

BROAD-BAND VERSUS NARROW-BAND MODELS

Four of the directivity models, sb13, sc13, row13, and cscy claim to be narrow-band, but sb13 is much narrower than the other three models. Figure 10 shows that for rv2, sb13 predicts high directivity at 1 s period that disappears entirely by 10 s. On the other hand, sc13 predicts directivity amplifications that is fairly flat between 3 and 10 s, and so can be called narrow-band only in the sense that directivity amplification does not rise inexorably as period increases, unlike Somerville et al. (1997) or Spudich and Chiou (2008). Models cscy and row13 are intermediate between the two.

This is not entirely surprising. Model sb13 is explicitly a model of the response spectrum of an impulsive ground motion, that is, it is a pulse model, and the pseudo-spectral velocity is known to peak at the pulse period, while the pseudospectral acceleration has a corner near the pulse period. Models sc13 and row13, on the other hand, included both impulsive and non-impulsive motions in their development, and thus are an average of the two.

The "strength" of "narrow-bandedness" in these models directly depends on the size (or the choice) of the bandwidth in the Magnitude-Pulse Period relation. In the Rowshandel and Spudich and Chiou models, for instance, the bandwidth for individual earthquakes was found
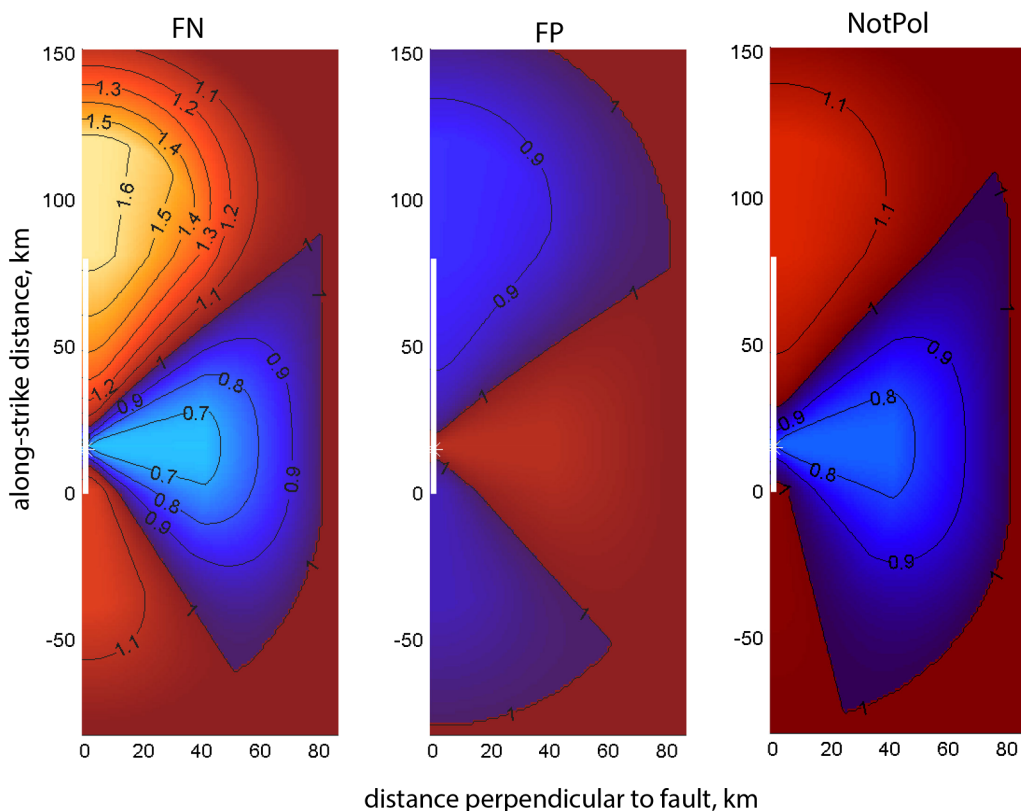
Figure 9. Directivity amplification in the FN, FP, and non-polarized (RotD50) components for test model ss3 for bay13 at 5 s period.

to be rather small (e.g., $< 0.1 - 0.4$), which would render the model(s) "very narrow band" if applied to individual earthquakes, which is the same as (or even narrower than) the sb13 model. However, moving from individual earthquakes to the entire residual data in NGA-West2, this bandwidth increases to 0.6 or 0.8 (or perhaps even more) in order to preserve the correlations (or linear fits) between directivity parameter(s) and ground motion residuals. It should also be noted that, in reality, a similar transition from "earthquakes-with-pulse" narrow bandwidth to overall (pulse and non-pulse earthquakes) larger bandwidth will have to take place in the sb13 model, when the probability of pulse (with a relatively flat probability density function) is superimposed on the "conditional" pulse-based narrow-band model. However, sb13's test case results include the probability of pulse and the distribution of T_p given $\mathbf{M}$ for each test case to get the expected value of amplification. So the bandwidth shown by the figure above includes the effect of uncertainties in those parameters.

COMPARISON OF DIRECTIVITY MODELS FOR CHI-CHI AND DENALI

Comparisons of the directivity models cscy, row13, sb13, and sc13 predictions for the 1999 $\mathbf{M}$ 7.6 Chi-Chi, Taiwan, and the 2002 $\mathbf{M}$ 7.9 Denali, Alaska, earthquakes (Figure 11)
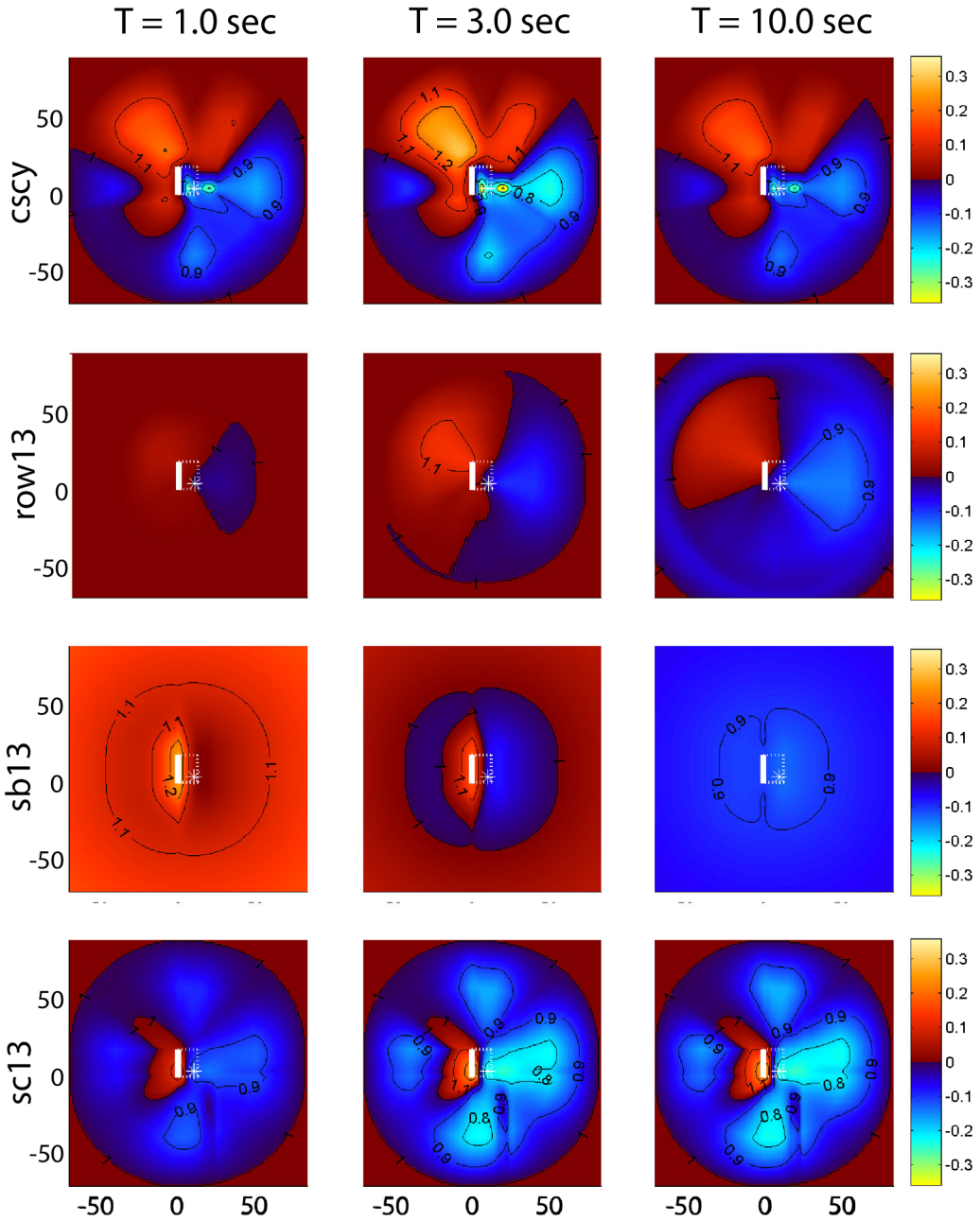
Figure 10. Example of four narrow-band directivity models: cscy (top row), row13 (second row), sb13 (middle), and sc13 (bottom row). Predictions are shown for 1 s, 3 s, and 10 s for rupture model rv2. Note that the sb13 model is much more sharply peaked in period than the others, in which the peak directivity value varies rather slowly between periods.
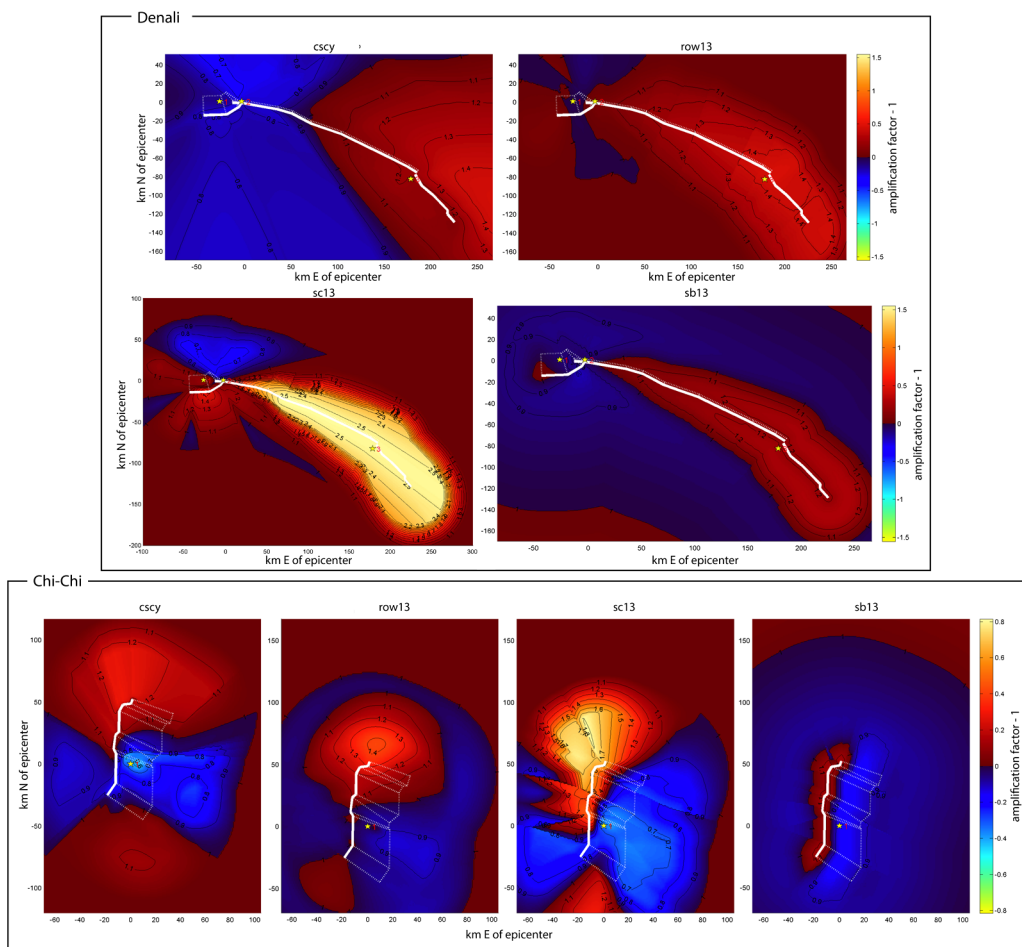
Figure 11. Directivity amplification at 5 s period for the 1999 Chi-Chi, Taiwan (lowest row), and the 2002 Denali, Alaska (upper rows), earthquakes. Solid white line is fault trace. Dashed white lines are surface projections of buried quadrilateral fault segments. The Chi-Chi rupture geometry is a single-fault (i.e., single-hypocenter) multi-segment rupture. Denali geometry consists of three multi-segment faults.

show some flaws in the directivity models when applied to ruptures with complicated geometries. (No result was available for bay13.)

For the Chi-Chi earthquake, contrary to our previous lamentations about the dissimilarity of directivity predictions for reverse faults, the three non-pulse models—cscy, row13, and sc13—produce fairly similar maps of directivity amplification. The pulse model, sb13, predicts pulses only close to the rupture trace with equal probability anywhere along the fault trace, so the pulse and non-pulse models disagree most strongly south of the epicenter.

The "stilettos" of directivity west of the fault trace in the sc13 model are caused by discontinuities in IDP (Figure 3) discussed earlier. All directivity models that depend on the closest point to a site will give spatially discontinuous predictions. Subtle discontinuities can be seen in the sb13 map, perhaps subtle because this directivity pulse model does not predict substantial enhancement more than about 10 km from the fault. The row13 predicted amplification is much smoother than those in the other models because the row13 prediction is an integral over the entire rupture area (see also Figure 3). The Chi-Chi rupture is modeled as a single-fault, multi-segment rupture.

Three of the four models (row13, sc13, and sb13) give similar maps of long "tongues" of amplification for the Denali earthquake (Figure 11). Surprisingly, for a rupture of this length even sb13 predicts pulses in a zone 50 km wide at the end of the rupture. This raises the question, however, of whether the assumed distance tapers in the directivity models are exerting excessive control. The width of the high-amplitude "tongue" in the sc13 result is certainly controlled by the distance taper from 40–70 km (Table 2). The factor controlling the width of the directivity tongue is not so clear in row13 and sb13. The sb13 map predicts approximately uniform pulse amplitude within 25 km of the fault at its southeast end. Of course, there are no strong motion data taken 25 km from a **M** 7.9 event, so for this event the sb13 model assumptions control the width of the distribution. (In fact, there are no data in this distance range from the **M** 7.5 Kocaeli, Turkey, earthquake, which is the second largest strike-slip event in the data set.) Ironically, row13, which does not bill itself as a pulse model, has the directivity amplification most strongly peaked at the fault. By contrast, bay13, which uses a distance taper extending to half the fault length, would have a much wider directivity tongue, as can be seen in Figure 5 for test model ss7.

The anomalous result is from cscy, for which the maximum directivity is displaced from the fault trace. This is caused by an error in the computational algorithm for multi-fault ruptures, in which at some sites the algorithm selects DPP from one fault and R_{RUP} from another closer fault. This is an inconsistency in the definition of f_D, but is not a systematic error affecting the Chiou and Youngs (2014) GMPE because only a small fraction of directivity data in NGA-West2 is affected. We report it here because this algorithm was used in Chiou and Youngs (2014).

SUMMARY AND CONCLUSIONS

Four teams of directivity modelers derived five improved directivity models by making conceptual advances as well as thorough empirical study of the expanded NGA-West2 data set. Among the conceptual advances was the adoption by some modelers of narrow-band directivity models. In addition, all models eschew normalized fault dimensions, because normalized fault dimensions cause nonphysical scaling of directivity for large magnitude events.

Comparisons show that the vertical strike-slip rupture geometries are modeled similarly by each directivity model, and there are many areas of agreement. However, for reverse faults the predicted motions differ from each other so much that it would be unwise to ignore the epistemic uncertainty and use just one directivity model to predict motions at a specific site.

After ten years of directivity model development associated with NGA-West1 and NGA-West2, these directivity models are certainly better than no directivity model, but they are still rather unsatisfying. Directivity can be clearly seen in PGA and PGV of earthquakes in the **M** 3–5 range (Boatwright 2007, Seekins and Boatwright 2010), but none of these models has a functional form that transitions smoothly from large to small magnitude and that describes the small-magnitude or short-period directivity. Of course, this may be of little engineering concern, but it indicates an unsatisfying omission of some important physical principle. Possibly the Shahi and Baker (2013) model is closest to being able to address this issue.

It is troubling that the width of high-directivity zones is controlled by rather poorly constrained distance tapers. This taper should be a function of period, but only the Rowshandel model addresses this issue. The comparison of the reverse-faulting predictions gives pause because of the previously mentioned sensitivity of the results to the assumptions of the model. For example, the use of a point source radiation pattern in the Spudich and Chiou model has clear effects that would probably not result from an extended finite source. It would be an advance to be able to approximate a finite-source radiation pattern, on which Chiou and Spudich (2013), following Watson-Lamprey (unpublished notes 2012), have taken some steps, rather than having to calculate it directly by integrating over the fault surface, as in Rowshandel (2013). It is also troubling that the big ground motion records that excited interest in directivity, like the Lucerne recording of the Landers earthquake, occur at short rupture distances and within the ends of the causative fault. Numerical simulations of ground motions on long strike-slip faults, as noted in Spudich and Chiou (2008), also show that the maximum motions occur within the ends of the faults, but our directivity models for strike-slip events tend to predict the biggest motions in a broad zone off the "shotgun" end of the fault, probably because they developed as corrections to GMPEs that already modeled much of the near-fault directivity with some other functions of **M** and R. It is possible that when directivity models are included ab initio in the development of a GMPE, the magnitude and distance terms may change dramatically. The Chi-Chi, Taiwan, main shock and aftershocks seem to ooze directivity, but very recent unpublished work (B. Chiou, *pers. communication*, 2013) suggests that associated with the seismic stations there are site amplifications that might mimic directivity, meaning that the directivity models presented here might be biased high. San Andreas–system earthquakes often have classic directivity pulses (e.g., 1979 Coyote Lake, 1984 Morgan Hill), but when a non-pulse directivity model is fit to all their recordings, the fit is poor. Fitting our current directivity models to Japanese crustal earthquake data is even more of a challenge. It might be that the physical wear process associated with cumulative offset of San Andreas system events may be greater than the same for Japanese earthquakes, and such wear has created low-velocity zones or other physical changes that enhance ground motions (e.g., Spudich and Olsen 2001).

APPENDIX

Please refer to the online version of this paper to access Appendix: How the Results Were Calculated.

REFERENCES

Aagaard, B. T., Hall, J. F., and Heaton, T. H., 2002. *Effects of Fault Dip and Slip Rake on Near-source Ground Motion: Why Chi-Chi Was a Relatively Mild M7.6 Earthquake*, PEER Report No. 2002/12, Pacific Earthquake Engineering Research Center, Berkeley, CA.

Abrahamson, N., 2000. Effects of rupture directivity on probabilistic seismic hazard analysis, in *6th Int. Conf. on Seismic Zonation, Proceedings: Earthq. Eng. Res. Inst. CD-2000-01*.

Abrahamson, N., and Silva, W., 2008. Summary of the Abrahamson and Silva NGA ground motion relations, *Earthuake Spectra* **24**, 67–97.

Ancheta, T. D., Darragh, R. B., Stewart, J. P., Seyhan, E., Silva, W. J., Chiou, B. S.-J., Wooddell, K. E., Graves, R. W., Kottke, A. R., Boore, D. M., Kishida, T., and Donahue, J. L., 2013. *PEER NGA-West2 Database*, PEER Report No. 2013/03, Pacific Earthquake Engineering Research Center, Berkeley, CA.

Bayless, J., and Somerville, P., 2013. *Bayless-Somerville Directivity Model*, Chapter 3 of PEER Report No. 2013/09, P. Spudich (Editor), Pacific Earthquake Engineering Research Center, Berkeley, CA.

Bizzarri, A., Dunham, E. M., and Spudich, P., 2010. Coherence of Mach fronts during heterogeneous supershear earthquake rupture propagation: Simulations and comparison with observations, *Journal of Geophysical Research: Solid Earth* **115**, 22 pp.

Boatwright, J., 2007. The persistence of directivity in small earthquakes, *Bull. Seismol. Soc. Am.* **97**, 1850–1861.

Boore, D. M., Watson-Lamprey, J., and Abrahamson, N. A., 2006. Orientation-independent measures of ground motion, *Bull. Seismol. Soc. Am.* **96**, 1502–1511.

Campbell, K. W., and Bozorgnia, Y., 2008. NGA ground motion model for the geometric mean horizontal component of PGA, PGV, PGD, and 5% damped linear elastic response spectra for periods ranging from 0.01 to 10 s, *Earthquake Spectra* **24**, 139–171.

Chiou, B. S.-J, and Spudich, P., 2013. The Chiou and Spudich Directivity Predictor DPP, in Chapter 6 of PEER Report No. 2013/09, P. Spudich (Editor), *Pacific Earthquake Engineering Research Center*, Berkeley, CA.

Chiou, B.S.-J., and Youngs, R. R., 2013. *Update of the Chiou and Youngs NGA Ground Motion Model for Average Horizontal Component of Peak Ground Motion and Response Spectra*, PEER Report No. 2013/07, Pacific Earthquake Engineering Research Center, University of California, Berkeley, CA, 76 pp.

Chiou, B. S.-J., and Youngs, R. R., 2014. Update of the Chiou and Youngs NGA model for the average horizontal component of peak ground motion and response spectra, *Earthquake Spectra* **30**, 1117–1153.

Das, S., 2010. Earthquake supershear rupture speeds, *Tectonophys.* **493**, 213–215.

Oglesby, D. D., Archuleta, R. J., and Nielsen, S. B., 2000. The three-dimensional dynamics of dipping faults, *Bull. Seismol. Soc. Am.* **90**, 616–628.

Rowshandel, B., 2010. Directivity correction for the Next Generation Attenuation (NGA) relations, *Earthuake Spectra* **26**, 525–559.

Rowshandel, B., 2013. Rowshandel's NGA-West2 directivity model, Chapter 3 of PEER Report No. 2013/09, P. Spudich (Editor), *Pacific Earthquake Engineering Research Center*, Berkeley, CA.

Schmedes, J., and Archuleta, R. J., 2008. Near-source ground motion along strike-slip faults: Insights into magnitude saturation of PGV and PGA, *Bull. Seismol. Soc. Am.* **95**, 2278–2290.

Seekins, L., and Boatwright, J., 2010. Rupture directivity of moderate earthquakes in northern California, *Bull. Seismol. Soc. Am.* **100**, 107–1119.

Shahi, S. K., 2013. A Probabilistic Framework to Include the Effects of Near-Fault Directivity in Seismic Hazard Assessment, Ph.D. Thesis, Stanford University, Stanford, CA, 226 pp.

Shahi, S. K., and Baker, J. W., 2011. An empirically calibrated framework for including the effects of near-fault directivity in probabilistic seismic hazard analysis, *Bull. Seismol. Soc. Am.* **101**, 742–755.

Shahi, S. K., and Baker, J. W., 2013. Shahi-Baker Directivity Model, Chapter 4 of PEER Report No. 2013/09, P. Spudich (Editor), Pacific Earthquake Engineering Research Center, Berkeley, CA.

Somerville, P. G., 2003. Magnitude scaling of the near fault rupture directivity pulse, *Phys. Earth Planet. In.* **137**, 201–212.

Somerville, P. G., Smith, N. F., Graves, R. W., and Abrahamson, N. A., 1997. Modification of empirical strong ground motion attenuation relations to include the amplitude and duration effects of rupture directivity, *Seismol. Res. Lett.* **68**, 199–222.

Spudich, P., Bayless, J. R., Baker, J. W., Chiou, B. S.-J., Rowshandel, B., Shahi, S. K., and Somerville, P. G., 2013. Final Report of the NGA-West2 Directivity Working Group, *Pacific Earthquake Engineering Research Center Report PEER-2013/09*, Berkeley, CA, 130 pp.

Spudich, P., and Chiou, B. S.-J., 2008. Directivity in NGA earthquake ground motions: Analysis using isochrone theory, *Earthquake Spectra* **24**, 279–298.

Spudich, P., and Chiou, B. S.-J., 2013. The Spudich and Chiou NGA-West2 directivity model, Chapter 5 of PEER Report No. 2013/09, P. Spudich (Editor), Pacific Earthquake Engineering Research Center, Berkeley, CA.

Spudich, P., and Olsen, K. B., 2001. Fault zone amplified waves as a possible seismic hazard along the Calaveras fault in central California, *Geophys. Res. Lett.* **28**, 2533–2536.